High-Performance THz Nano-Metamaterial Absorber with Negative Permittivity (0.1–10 THz) for Early Cancer Detection via Circulating Exosomes

Musa N. Hamza, Mohammad Tariqul Islam, Sunil Lavadiya, Iftikhar ud Din, Bruno Sanches, Slawomir Koziel, Syeda Iffat Naqvi, Abinash Panda, Mohammad Alibakhshikenari, B. Virdee, Ali Farmani, Peiman Parand, Salahuddin Khan, MD. Sipon Miah, and Md. Shabiul Islam

***Abstract*— Cancer remains one of the leading causes of mortality worldwide, with nearly 10 million cancer-related deaths and approximately 30 million new cases projected by 2030. While significant advances have been made in therapeutic strategies, such as targeted treatments, immunotherapy, and gene therapy, early diagnosis remains crucial for improving patient outcomes. However, conventional diagnostic tools like magnetic resonance imaging (MRI), computed tomography (CT), and histopathology often suffer from limited sensitivity and specificity. Emerging technologies, including liquid biopsy, nano-photonics, and terahertz (THz) sensing, offer promising alternatives by enabling faster, more accurate detection. In particular, extracellular vesicles (EVs)—specifically exosomes, which are nanometer-sized vesicles involved in cancer progression—have gained attention as biomarkers for early-stage cancer detection. Traditional methods for detecting exosomes typically rely on labeling with antibodies or dyes, which can be costly, time-consuming, and prone to false positives. This study presents a novel THz nano-metamaterial absorber designed for early cancer detection through circulating exosomes. The absorber features ultra-wideband operation from 0.1 to 10 THz and achieves absorption rates exceeding 92%, demonstrating exceptional sensitivity and precision. With a compact footprint of 100 × 100 nm² and a thickness of just 30 nm, the design incorporates silver (Ag) resonators, dual dielectric substrates (silicon dioxide [SiO_2] and titanium dioxide [TiO_2]), and a nickel (Ni) backplane. This configuration enables optimized plasmonic and dielectric interactions for effective electromagnetic wave absorption. Key performance features include polarization insensitivity, reduced noise, and the ability to achieve negative permittivity at 4.85 THz—enhancing the sensor's responsiveness to subtle refractive index changes in nanoscale biological samples such as cancerous exosomes. Comprehensive numerical analyses, including field distributions, surface currents, and scattering parameters, validate the sensor's performance. Benchmark comparisons highlight the proposed sensor's superior absorption efficiency, sensitivity, and nanoscale precision, setting a new standard for non-invasive, early-stage cancer diagnostics.**

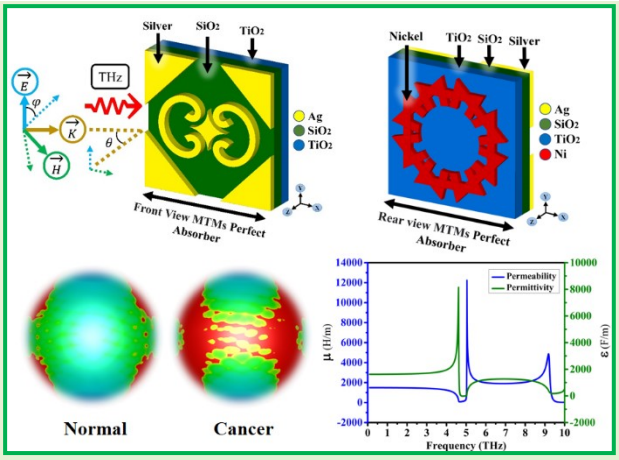

***Index Terms*— Biosensors, cancer diagnostics, terahertz imaging, circulating exosomes, perfect absorber metamaterials, nano-sensor.**

I. Introduction

The authors gratefully acknowledge the financial support of the University of Doha for Science and Technology under Grant No. KK-2024-005. Additionally, part of this research has been supported by the Icelandic Research Fund (Grant No. 239858), by the National Science Centre of Poland (Grant No. 2020/37/B/ST7/01448) and by Researchers Supporting Project number (RSP2024R58), King Saud University, Riyadh, Saudi Arabia. (Corresponding authors: Musa N. Hamza ; Mohammad Tariqul Islam; Mohammad Alibakhshikenari; Md. Shabiul Islam)

Musa N. Hamza is with Department of Physics, College of Science, University of Raparin, Sulaymaniyah 46012, Iraq. (e-mail: musa.nuraden@uor.edu.krd)

Mohammad Tariqul Islam is with Department of Electrical, Electronic and Systems Engineering, Faculty of Engineering and Built Environment, Universiti Kebangsaan Malaysia, 43600 UKM Bangi, Selangor, Malaysia. (e-mail: tariqul@ukm.edu.my)

Sunil Lavadiya is with Department of Information and Communication Technology, Marwadi University, Rajkot-360003, Gujarat, India. (e-mail: sunil.lavadiya@marwadieducation.edu.in)

Iftikhar ud Din is with Telecommunication Engineering Department, University of Engineering and Technology, Mardan 23200, Pakistan. (e-mail: iftikharuddin114@gmail.com)

Bruno Sanches is with Department of Electronic Systems Engineering, Escola Politécnica da Universidade de São Paulo São Paulo, Brazil. (e-mail: bruno.csanches@usp.br)

Slawomir Koziel is with Engineering Optimization & Modeling Center, Reykjavik University, 102 Reykjavik, Iceland.

Slawomir Koziel is also with Faculty of Electronics, Telecommunications and Informatics, Gdansk University of Technology, 80-233 Gdansk, Poland. (e-mail: Koziel@ru.is)

Syeda Iffat Naqvi is with Department of Telecommunication Engineering University of Engineering & Technology Taxila, Pakistan. (e-mail: iffat.naqvi@uettaxila.edu.pk)

Abinash Panda is with Department of Electronics and Communication Engineering, CMR Institute of Technology, Bengaluru 560037, India. (e-mail: abinashpanda087@gmail.com)

Mohammad Alibakhshikenari and Peiman Parand are with the Electronics Engineering Department, University of Rome "Tor Vergata", 00133 Rome, Italy. (e-mail: alibakhshikenari@ing.uniroma2.it; peiman.parand@students.uniroma2.eu)

Bal Virdee is with Department of Center for Communications Technology, London Metropolitan University, London N7 8DB, United Kingdom; (e-mail: b.virdee@londonmet.ac.uk)

Ali Farmani is with Department of electronics engineering, Lorestan University, Iran. (e-mail: farmani.a@lu.ac.ir)

Salahuddin Khan is with College of Engineering, King Saud University, P.O.Box 800, Riyadh 11421, Saudi Arabia; (e-mail: drskhan@ksu.edu.sa)

MD. Sipon Miah is with Department of Signal Theory and CommunicationsUniversity Carlos III of Madrid, Leganes, Madrid, Spain; (e-mail: mmiah@ing.uc3m.es)

MD. Sipon Miah is with Department of Information and Communication Technology, Islamic University, Kushtia, 7003, Bangladesh; (e-mail: sipon@iu.ac.bd)

Md. Shabiul Islam is with Centre for Advanced Devices and Systems, Faculty of Artificial Intelligence and Engineering, Multimedia University, Persiaran Multimedia, 63100 Cyberjaya, Selangor, Malaysia. (e-mail: shabiul.islam@mmu.edu.my)

Cancer remains a significant global health challenge with an estimation of 17 million cancer-related deaths and 26 million new diagnoses by 2030 [1, 2]. The fight against cancer has become multifaceted, involving early detection, effective treatments, and the exploration of cutting-edge therapies. A central part of these efforts is the development of advanced diagnostic technologies, which enable earlier and more accurate detection of cancer, as well as the development of more personalized and effective treatment options [3]. Several evolving technologies and strategies such as liquid biopsy involving Circulating Tumor DNA (CTDNA), Circulating Tumor Cells (CTCs), and Circulating Cancer Exosomes, optical sensing, multi-omics approaches, as well as microfluidics-based platforms are driving progress in this area. Exosomes are small vesicles typically 30–150 nanometers in diameter secreted by cells including tumor cells, that contain proteins, lipids, and nucleic acids. These exosomes can carry molecular signatures of tumors, and their analysis offers potential for early cancer detection and monitoring of disease progression [4].

Unlike traditional biopsies, which require tissue samples from the tumor, the liquid biopsy with exosomes offers a non-invasive alternative. A blood or urine sample is enough to collect these exosomes, avoiding the need for surgery or invasive procedures. Exosomes are shed into the bloodstream or other body fluids at early stages of cancer development, even before tumors are detectable via traditional imaging techniques like CT scans or MRIs. The quantity and molecular content of circulating exosomes can change in response to the presence of cancer, enabling detection at much earlier stages when treatments are often more effective [5, 6]. Exosome detection typically involves labeling methods utilizing antibodies or dyes or other markers that target specific surface proteins on these tiny vesicles. Methods like these are pretty effective but they present several challenges, including high costs, time consumption, and potential for false positives due to non-specific binding [7]. To overcome these limitations, new innovative technologies have emerged that offer higher sensitivity, specificity, and cost-efficiency. Techniques like plasmonic and nano-sized metamaterial-based sensors allow for direct detection of exosomes without the need for antibodies or dyes. These sensors rely on detecting physical properties such as refractive index changes or scattering signals caused by the presence of exosomes. Signal amplification property of Nano-metamaterials facilitates the efficient binding resulting in enhanced sensitivity and specificity of exosome detection [8].

Metamaterials (MMs) are artificially engineered materials that exhibit extraordinary electromagnetic properties, enabling capabilities far beyond those of natural materials. These properties, such as negative permittivity (ε), negative permeability (μ), and even negative refractive index (NRI), arise from their uniquely structured subwavelength elements rather than their chemical composition [9, 10]. Epsilon-negative (ENG) materials, a subset of metamaterials, are characterized by their unique property of having a negative dielectric permittivity ($\varepsilon < 0$) at certain frequencies. ENG materials achieve negative permittivity through tailored structures (e.g., split-ring resonators, thin-wire arrays) rather than natural material properties. This property allows them to support unique electromagnetic phenomena such as evanescent wave amplification, which enhances their sensitivity in detecting biomolecular interactions [11]. Thus, the versatility of metamaterials (MMs) has resulted in a diverse spectrum of engineering applications, spanning across industries, from telecommunications and bio-sensing to defense and energy [12–44]. ENG biosensors usually rely on resonance-based methods for detection purposes. ENG material surfaces are treated with antibodies or aptamers that latch onto cancer biomarkers like PSA for prostate cancer or HER2. Upon introduction of a sample with biomarker, biomarker adheres to functionalized surface thereby altering refractive index locally. ENG material significantly amplifies changes in evanescent wave resonance frequency caused by refractive index shift somehow. Detected signal magnitude correlates directly with biomarkers such as proteins, DNA, or circulating tumor cells, thereby facilitating precise quantification through analysis [45].

Recent literature has highlighted the promise and challenges of using photonic platforms for liquid biopsy applications. A comprehensive review by Dell'Olio et al. [46] outlines recent advances in photonic biosensors—including plasmonic and interferometric technologies—for detecting circulating biomarkers such as exosomes. Additionally, several emerging metasurface designs have demonstrated ultra-narrowband sensitivity by exploiting bound states in the continuum (BIC) resonances. For instance, Algorri et al. have proposed polarization-independent nanocuboid metasurfaces supporting quasi-BIC modes [47] and experimentally demonstrated silicon-slot metasurfaces capable of BIC-based sensing in the near-infrared [48]. While such structures offer remarkable detection sensitivity, they are often limited to narrowband operation and may face fabrication or alignment complexity. In contrast, the proposed terahertz (THz) nano-metamaterial absorber in this study offers ultra-broadband performance (0.1–10 THz), polarization insensitivity, and nanoscale compactness—making it well-suited for real-world, label-free cancer diagnostics using circulating exosomes.

Many conventional sensors lack the precision to detect low concentrations of biomolecules, which is critical for early diagnosis and monitoring of diseases. Also, traditional sensors often lack flexibility for diverse applications. The advancements in technology and challenges in clinical validation emphasize the need for more compact and effective nano-sized metamaterial absorbers enabling nano bio-sensing systems for disease detection and health monitoring [49]. The ability of nano-metamaterials to confine electric and magnetic fields enhances their interaction with target analytes, enabling the detection of trace amounts of substances such as DNA, proteins, or pathogens. Moreover, Nano-metamaterial biosensors provide real-time responses by directly detecting biomolecular interactions without requiring extensive labeling or preparation. In addition, Nano-metamaterial-based biosensors are adaptable to a wide range of frequencies e.g., optical and Terahertz (THz) making them suitable for healthcare, early cancer diagnosis [12–18, 20–32, 34–36], environmental monitoring, food safety, and drug development. However, this sensor miniaturization moved the

communication from low frequency ranges to higher frequencies such as THz [50, 51].

The terahertz (THz) wave band possesses all advantageous characteristics in biomedical applications. THz waves are very low energy that do not cause ionization or damage to living tissues and the human body, therefore guaranteeing safety for medical imaging and diagnostics. Additionally, many biological macromolecules and polar molecules have THz energy levels of vibration and rotation, so that this resonance enables the specific interaction of THz waves with these molecules, making it a very powerful tool for characterizing biological tissues [35, 52]. As a result, since THz waves have distinct interactions with biological molecules, THz spectroscopy can be leveraged for a diversity of medical diagnostic applications without requiring invasive procedures. Terahertz (THz) spectroscopy, particularly in the frequency range of 0.1–10 THz has attracted considerable attention for its potential applications in biomedical analytics, detection, imaging, trapping, and sensing. Being label-free, non-contact, and non-destructive, its advantages render it very attractive for medical diagnostics [53, 54].

While nano-scaled ENG metamaterial-based biosensors hold great promise for revolutionizing cancer diagnostics through the detection of circulating exosomes, several challenges need to be addressed to make them suitable for widespread clinical use. By focusing on improving sensitivity, specificity, exosome isolation methods, cost-effectiveness, and integration into existing healthcare systems, these biosensors could become a valuable tool for early cancer detection, real-time monitoring, and personalized treatment. Hence, the development of absorbers with simple nanoscale structures and high absorption rates remains a critical area of research due to their wide-ranging practical applications for bio-sensing. This article proposes a nano-metamaterial based THz absorber for the frequency range 0.1–10 THz with negative permittivity for early detection of cancer using circulating exosomes. The proposed absorber exhibits polarization insensitivity, guaranteeing that the sensor maintains consistent performance regardless of the polarization state of the incident THz radiation. At a specific frequency of 4.85 THz, the sensor exhibits negative permittivity ($\varepsilon < 0$), a property that significantly enhances the sensitivity to subtle variations in the refractive index of biological samples, such as circulating exosomes. The high sensitivity and wide frequency range of the proposed sensor ensure that even small quantities of exosomes can be detected, making it an ideal candidate for early cancer detection applications.

II. Structural Design of Metamaterials (MTMs) and Electromagnetic Field Configuration

The proposed metamaterial perfect absorber features an innovative multi-layered nano-scale configuration, designed to achieve superior absorption characteristics across the terahertz (THz) spectrum (0.1–10 THz). Its structure ensures polarization insensitivity and achieves absorption efficiencies exceeding 92%, making it highly suitable for biosensing applications, particularly for early cancer detection.

At the top of the structure lies the resonator layer, composed of silver (Ag), chosen for its excellent conductivity and plasmonic behavior at THz frequencies. This layer is 5 nm thick and plays a key role in facilitating strong interactions with incident electromagnetic waves.

Beneath the resonators is the first dielectric substrate, a 10 nm thick layer of silicon dioxide (SiO_2), which provides structural support and aids in wave propagation. This is followed by a second 10 nm layer of titanium dioxide (TiO_2), which complements SiO_2 by enhancing electromagnetic resonance across the target frequency range.

The ground plane is constructed using a 5 nm thick nickel (Ni) layer. Unlike conventional absorbers that typically use a fully covered ground plane, the use of nickel introduces advantageous electromagnetic properties and structural durability. Its presence enhances the absorber's efficiency by effectively interacting with reflected waves and minimizing transmission losses.

This layered configuration allows the metamaterial to exhibit unique electromagnetic properties, including negative permittivity ($\varepsilon < 0$) at 4.85 THz—an essential characteristic for biosensing applications such as exosome detection.

For performance validation, CST Studio was used to carry out precise electromagnetic simulations. Appropriate boundary conditions, including Perfectly Matched Layers (PMLs), were implemented to eliminate undesired reflections and ensure accurate energy confinement. Additionally, fine meshing was applied around the resonators to capture detailed field interactions, leading to a highly accurate representation of the absorption mechanisms.

This meticulous design and simulation process underlines the metamaterial absorber’s potential as a transformative tool for nanoscale biosensing, offering exceptional performance throughout the THz range.

A. Structural Design of Metamaterials (MTMs)

The shape and geometry of the proposed structure play a critical role in optimizing energy absorption. Minimizing reflection from the surface directly enhances the absorber's efficiency. In designing any biosensor, three primary parameters must be considered: selectivity, specificity, and sensitivity. Leveraging metamaterial properties is essential for enhancing these performance metrics.

By enabling precise control over the interaction between electromagnetic waves and the structure, the metamaterial-based design addresses key challenges in biosensor sensitivity and specificity.

The front view of the proposed structure is illustrated in Figure 1. The initial resonator layout, shown in Figure 1(a), features four resonators positioned at each corner. Each resonator has a length D, width A, and is spaced from adjacent elements by a gap B. The equilateral triangular component has a side length C. The alternative resonator layout, presented in Figure 1(b), includes two mirror-arranged C-shaped resonators, each with length E and width F. The gap between the terminals of each resonator is G. The final resonator configuration, shown in Figure 1(c), introduces a central cross-triangle-shaped resonator positioned between two centrally located resonators. All resonators are composed of silver (Ag) and are mounted on a silicon dioxide (SiO_2) substrate. The resonator size is denoted by I, and the overall structure dimensions are H × H.

The rear view of the design is presented in Figure 2. This layer features resonators made of nickel (Ni), mounted on a titanium dioxide (TiO_2) substrate. The novel circular resonator design incorporates strategic cuts and shaping, which contribute to the metamaterial behavior of the structure. The diameter of each circle is K, with inter-element spacing L, and a gap J between resonators spaced at 90 degrees.

All geometric dimensions and parameters are summarized in Table 1.

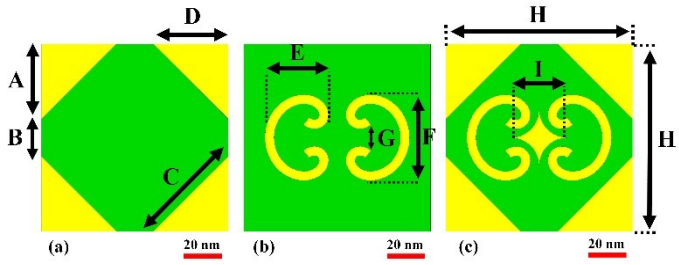

Figure 1: Diagram showcasing the proposed nano-metamaterial perfect absorber, emphasizing the frontal view and arrangement of silver resonators: (a) Initial resonator design, (b) Alternate resonator layout, (c) Finalized resonator configuration.

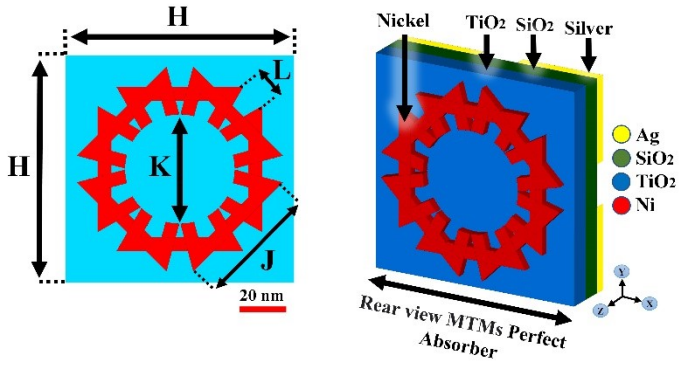

Figure 2: Diagram illustrating the rear perspective of the nano-metamaterial absorber, emphasizing the nickel backplane and overall design concept.

B. Electromagnetic Field Configuration and Absorption Mechanism

The metamaterial absorber operates across the terahertz (THz) spectrum from 0.1 to 10 THz, an ideal frequency range for biosensing due to its ability to non-invasively probe biological tissues. This range is particularly effective for detecting biomarkers such as exosomes, which are crucial for early cancer diagnosis.

The absorber's structure incorporates a multi-layered design, with each component contributing to its high-performance functionality. The resonator layer consists of silver (Ag) and features a central diamond-shaped element alongside C-shaped and triangular structures. Silver enables strong surface plasmon resonance, enhancing electromagnetic interaction at the nanoscale.

Beneath the resonators are two dielectric substrates: a 10 nm-thick layer of silicon dioxide (SiO_2), which supports impedance matching, and a 10 nm-thick layer of titanium dioxide (TiO_2), selected for its durability, high refractive index, and chemical stability—qualities essential for consistent THz sensing. The base layer is a 5 nm-thick nickel (Ni) ground plane. Unlike traditional continuous ground layers, this design reduces reflection and improves overall absorption.

The interaction of THz waves with the structure aligns the electric field ($\vec{E}$), magnetic field ($\vec{H}$), and wave vector ($\vec{k}$) with the resonators, generating effective resonance and maximizing absorption. Fine-tuning angular parameters enhance field confinement, improving energy conversion and minimizing reflection and transmission thereby increasing biosensing sensitivity.

Precise optimization of the structure's geometry and material thicknesses ensures resonance at target frequencies, broad operational bandwidth, and absorption efficiency exceeding 92% across the THz range.

This innovative multi-layered design, combining advanced materials and geometric precision, offers a promising platform for early-stage cancer detection and other high-sensitivity biomedical diagnostics.

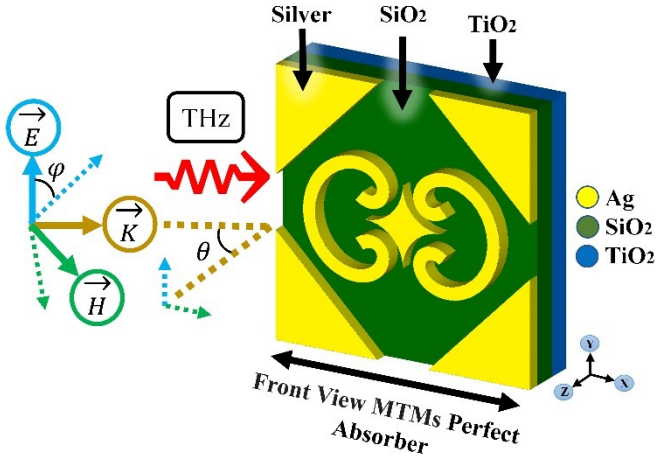

Figure 3: Depiction of the absorber's structural configuration, demonstrating the alignment of the incident electromagnetic field to achieve optimal absorption.

TABLE 1: COMPREHENSIVE SUMMARY OF OPTIMIZED VARIABLES FOR THE PROPOSED NANO-METAMATERIAL PERFECT ABSORBER.

Parameter	Dimensions (nm)	Parameter	Dimensions (nm)
A	40	I	30
B	20	J	55.43
C	56.57	K	48
D	40	L	11.72
E	33.7	Ag Thick	5
F	45	SiO_2 Thick	10
G	13.75	TiO_2 Thick	10
H	100	Ni Thick	5

III. OPTIMIZATION AND PERFORMANCE ANALYSIS OF ABSORPTION CHARACTERISTICS

Optimizing absorption performance is essential for improving the functionality of nano-metamaterial perfect absorbers (Nano-MTMPAs). This section presents a detailed analysis of structural variations, substrate material selection, and resonator

design parameters to evaluate their effects on absorption efficiency. The findings offer valuable insights into how design and material choices influence the absorber's performance and contribute to achieving optimal absorption characteristics.

A. Comparative Evaluation of Structural Designs

Figure 4 presents a comparative analysis of the absorption responses of two model structures, with their respective performance illustrated in Figures 4(a) and 4(b). Absorption characteristics were evaluated across a wide frequency range from 0 to 10 THz, revealing distinct differences between the two models.

Model 1, shown in Figure 4(a), demonstrates highly efficient absorption, achieving a peak of 100% between 0 and 1.5 THz. From 1.5 to 6 THz, absorption slightly declines but remains strong at approximately 97%. Beyond 6 THz, the absorption stabilizes with minimal variation, maintaining 91% at 10 THz. These results indicate that Model 1 performs well over a broad frequency range, with only a modest reduction at higher frequencies.

Model 2, depicted in Figure 4(b), exhibits superior performance. It maintains 100% absorption from 0 to 2 THz and 97% from 2 to 6 THz. Even in the higher frequency range (6–10 THz), Model 2 shows improved stability, reaching 93% absorption at 10 THz. This demonstrates enhanced efficiency, particularly at lower frequencies.

Overall, the comparison highlights Model 2's more consistent and efficient absorption across the entire THz spectrum, making it a stronger candidate for broadband biosensing applications.

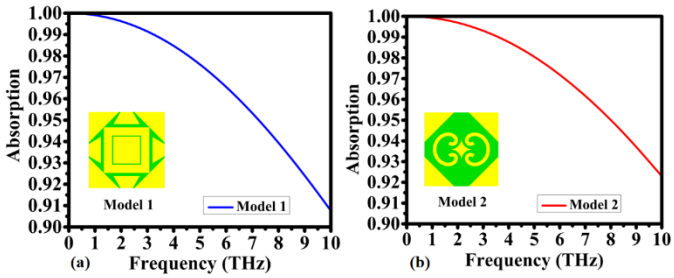

Figure 4: Comparison of absorption performance for different structural designs: (a) Absorption characteristics of design 1, (b) Absorption characteristics of design 2.

B. Impact of Material and Design Parameters on Absorption Efficiency

Figure 5 presents a spectral analysis of absorption efficiency, focusing on how variations in substrate thickness influence the performance of the nano-metamaterial absorber. The analysis is divided into two plots: Figure 5(a) investigates the effect of SiO_2 substrate thickness (10–100 nm), while Figure 5(b) examines the same range for TiO_2 substrates.

In Figure 5(a), variations in SiO_2 thickness lead to noticeable shifts in spectral absorption efficiency. As a low-refractive-index material, SiO_2 primarily affects interference patterns within the structure. Thin layers (10–30 nm) enhance absorption at shorter wavelengths due to constructive interference. In contrast, thicker layers (40–100 nm) shift the peak absorption to longer wavelengths, increasing the optical path length and altering resonance conditions. Notably, at 100 nm, the absorber reaches an efficiency of 91% at the upper frequency limit.

In Figure 5(b), the impact of TiO_2 thickness on absorption shows a distinct trend. Both very thin (10 nm) and very thick (100 nm) TiO_2 layers yield peak absorption efficiencies of 95%, indicating strong coupling of incident light into resonant modes and efficient light trapping. However, in the intermediate range (20–90 nm), absorption efficiency decreases progressively: 90% at 20 nm, 85% at 30 nm, 80% at 40 nm, 75% at 50 nm, 70% at 60 nm, 65% at 70 nm, 60% at 80 nm, and 55% at 90 nm.

This decline suggests that intermediate thicknesses are suboptimal for effective light confinement and resonance generation. In this range, interference effects and light-trapping mechanisms are less efficient, leading to reduced absorption performance.

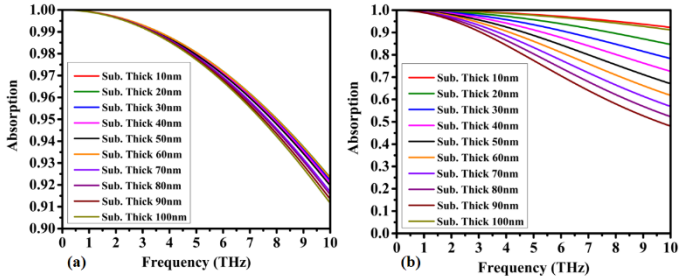

Figure 5: Spectral analysis of absorption efficiency for varying substrate thicknesses: (a) Effect of SiO_2 substrate thickness, (b) Effect of TiO_2 substrate thickness.

Figure 6(a) shows the effect of resonator material thickness on the absorber's performance. When the thickness of the resonating material ranges between 5 and 10 nm, perfect absorption (100%) is achieved in the 0–2 THz range, indicating effective absorption of electromagnetic waves at lower frequencies. As the frequency increases from 2 to 6 THz, absorption remains high at approximately 97%. However, further increases in thickness lead to a slight decline in efficiency—dropping to 94% at 8 THz and 92% at the upper frequency limit of 10 THz.

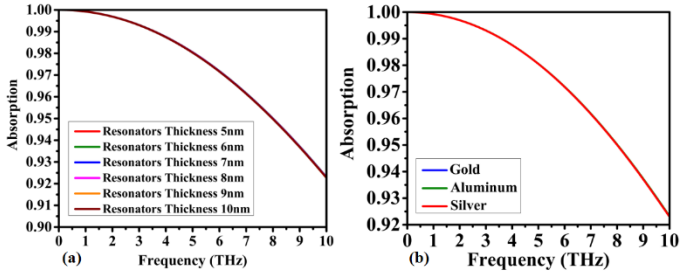

Figure 6: Influence of design variables on absorption efficiency: (a) Variations in resonator thickness, (b) Spectral response for different resonator materials.

Figure 6(b) presents the absorption characteristics of the proposed model using different resonating materials, including gold, aluminum, and silver. All three metals exhibit excellent absorption performance across a broad frequency range, achieving 100% absorption from 0 to 2 THz and maintaining

around 97% from 2 to 6 THz. From 6 to 8 THz, absorption remains strong at 95%, with a slight decrease to 92.5% at 10 THz.

These high absorption characteristics are attributed to the unique electronic configurations and plasmonic behaviors of the materials. The excellent conductivity and reflectivity of gold, aluminum, and silver allow them to interact strongly with incident electromagnetic waves. Their performance is primarily driven by surface plasmon resonance, where conduction electrons oscillate in sync with the incoming THz waves, enabling efficient energy absorption.

IV. Optimization of Metamaterial Structure and Absorption Performance

Understanding the electromagnetic characteristics of the absorber is crucial for optimizing its performance. This section examines the structure's permittivity (ε) and permeability (μ), along with key simulated parameters such as refractive index (n) and impedance. Additionally, the electromagnetic response including reflection, absorption spectra, and S-parameter behavior is analyzed to assess the absorber's efficiency and functionality under various conditions. These evaluations provide a comprehensive understanding of the absorber's operational principles and performance capabilities.

A. Electromagnetic Characteristics of the Absorber

When a terahertz (THz) wave is incident on the metamaterial (MTM) structure, a significant portion of the wave couples to the surface through light–matter interaction. Because the structure operates in the THz frequency range, its absorption characteristics are a key indicator of overall system performance. As such, analyzing the structure's optical properties is essential.

To investigate how frequency variations affect these properties, the frequency was swept from 0 to 10 THz in 1 THz increments, while other parameters were held constant. Both the real and imaginary components of permittivity (ε) and permeability (μ) were examined, as illustrated in Figure 7. A noteworthy finding is the presence of negative values in the imaginary part of permittivity, which suggests metallic behavior at certain frequencies.

Figure 7 presents the electromagnetic characteristics of the absorber. In Figure 7(a), negative permittivity ($\varepsilon < 0$) is observed at 4.85 THz—a key frequency associated with enhanced sensor sensitivity. This negative permittivity facilitates the excitation of surface plasmon polaritons, intensifying the interaction between incident THz waves and biological samples such as circulating exosomes. The resulting field confinement near the sensor surface significantly improves detection capabilities, particularly for low-concentration biomarkers related to early-stage cancer—targets that are often undetectable using conventional diagnostic methods.

The imaginary component of permittivity, shown in Figure 7(b), reflects energy dissipation within the material, which contributes to efficient wave absorption. Together, these electromagnetic properties enable the sensor to achieve high precision and sensitivity, making it well-suited for early cancer detection and other high-performance biosensing applications.

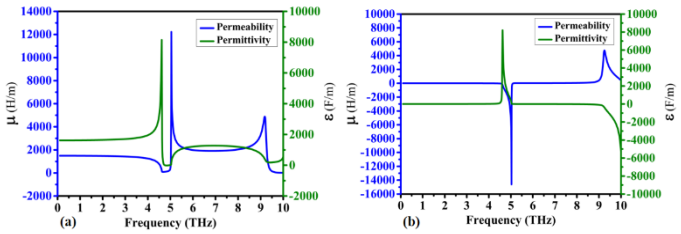

Figure 7: Electromagnetic properties of the absorber: (a) Real components of permittivity (ε) and permeability (μ), (b) Imaginary components of ε and μ.

To gain deeper insight into the absorber's behavior, we analyzed how its optical parameters influence absorption characteristics. Specifically, we examined the effects of frequency on the real and imaginary parts of both the refractive index and impedance. The frequency was varied from 1.0 to 10 THz in 1 THz increments for this analysis.

Figures 8(a) and 8(b) illustrate the relationship between frequency and the real and imaginary components of refractive index and impedance. The results show strong consistency with the previously discussed electromagnetic properties presented in Figure 7, confirming the accuracy and reliability of the simulation data.

These findings indicate that the resonance frequency of the structure is directly linked to its optical properties, which in turn govern the absorption spectrum. This relationship highlights the critical role of refractive index and impedance in tuning the absorber's performance.

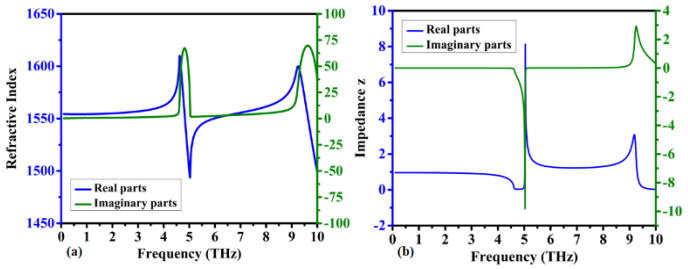

Figure 8: Numerical simulation of critical parameters: (a) Refractive index components (real and imaginary), (b) Impedance (Z) behavior.

B. Electromagnetic Response and S-Parameter Analysis

The proposed perfect absorber was simulated and evaluated in terms of reflectivity and absorption across a frequency range up to 10 THz. Figure 9(a) presents both the absorption and reflectivity results. The absorber exhibits very low reflectivity in the lower frequency range, with a gradual linear increase up to 10 THz. In contrast, it maintains a stable absorption profile, beginning with near-perfect absorption and consistently remaining above the standard threshold of 0.8—indicating strong performance across the spectrum.

To provide a more detailed view, Figure 9(b) presents a vertically scaled version of the absorption curve, along with the absolute value of the S11 scattering parameter (reflection coefficient). The S11 values remain very low up to 2 THz,

indicating excellent impedance matching and minimal reflection. Around 6 THz and above, some moderate reactive behavior is observed, but it remains within acceptable limits. Overall, these results confirm that the absorber performs effectively across the full 0–10 THz frequency range.

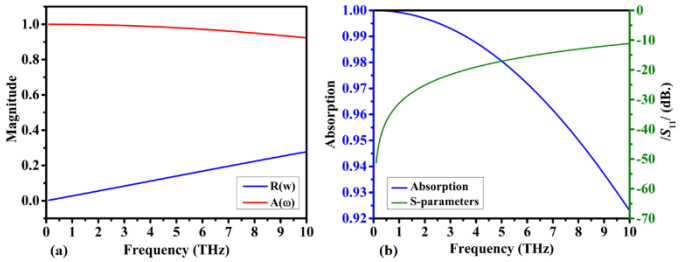

Figure 9: Simulated electromagnetic response: (a) Reflection and absorption spectra, (b) S-parameter performance ($|S_{11}|$ in dB).

Figure 10(b) displays the S_{21} curve, which corresponds to the transmitted portion of the wave passing through the absorber. A key design goal was to minimize transmission (or energy leakage) and maximize absorption. The results show negligible transmission below 2 THz. Although the transmission slightly increases and peaks around 9 THz, the optimized back layer design ensures that maximum transmission remains below 0.2%, a remarkably low value given the wide operational bandwidth.

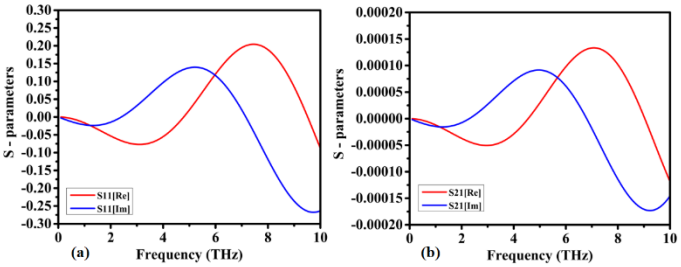

Figure 10: Detailed simulation results: (a) Real and imaginary components of S_{11}, (b) Real and imaginary components of S_{21}.

The absorption performance is exceptional throughout the spectrum, consistently achieving values above 0.92. The S_{11} curve further confirms this high performance, showing reflection values below –10 dB across the entire band, with initial values as low as –50 dB. These figures validate the effectiveness of the device over the full proposed bandwidth.

To provide a more comprehensive analysis of the sensor's scattering behavior, the complex S_{11} and S_{21} parameters are evaluated and plotted in Figure 10.

The next section will present a detailed analysis of the internal electromagnetic fields and surface current distributions within the absorber, shedding light on the core working mechanisms of the proposed sensor.

V. Field Distributions, Surface Currents, and Angular Dependence

A thorough analysis of electric and magnetic field distributions, surface currents, and angular dependence provides critical insights into the operational efficiency of the proposed absorber. This section investigates the spatial distribution of the electric (|E|) and magnetic (|H|) fields for both the silver resonators and the nickel backplane, including their real and imaginary components. Additionally, surface current distributions are visualized for both layers to better understand their roles in the absorption mechanism. Finally, the effects of angular variations such as incident and polarization angles on absorption efficiency are examined to evaluate the absorber's performance under diverse operating conditions.

A. Electric and Magnetic Field Visualization

Figure 11 shows the distribution of the electric field (|E|) for the silver resonators, including both real and imaginary components. The real component, illustrated in Figure 11(a), highlights the spatial intensity of the electric field associated with energy storage and resonance. The color gradient reveals strong field concentrations around the edges and curved sections of the resonators. The imaginary component, shown in Figure 11(b), represents the dissipative part of the electric field, crucial for understanding energy loss and absorption dynamics. High-intensity regions near the resonator's intricate features indicate strong interactions with incident terahertz waves. These simulations demonstrate the resonators' role in achieving high field confinement and efficient energy absorption.

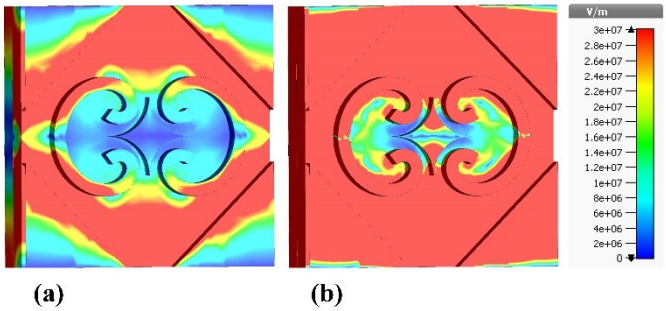

Figure 11: Distribution of the electric field (|E|) for silver resonators: (a) Real component of |E|, (b) Imaginary component of |E|.

Figure 12 presents the magnetic field (|H|) distribution for the silver resonators. In Figure 12(a), the real component reveals areas of magnetic energy storage and resonance, with significant enhancement around the curved regions of the structure. Figure 12(b) displays the imaginary component, highlighting the dissipative magnetic field associated with energy loss. The strongest |H| fields are observed near the inner edges of the resonators, supporting effective absorption mechanisms that enhance the absorber's overall performance.

Figure 13 illustrates the electric field distribution on the nickel backplane. Figure 13(a) shows the spatial intensity of the real component, with concentrated fields around detailed structural features. These areas indicate how the backplane reflects and amplifies incident electromagnetic waves, improving field confinement and contributing to absorption efficiency. Figure 13(b) displays the imaginary component, representing areas of energy dissipation within the nickel layer. High field intensities in specific regions signal effective absorption and loss mechanisms critical to the absorber's function.

This rear-view analysis underscores the nickel backplane's dual role: enhancing field confinement and facilitating energy dissipation to achieve near-perfect absorption.

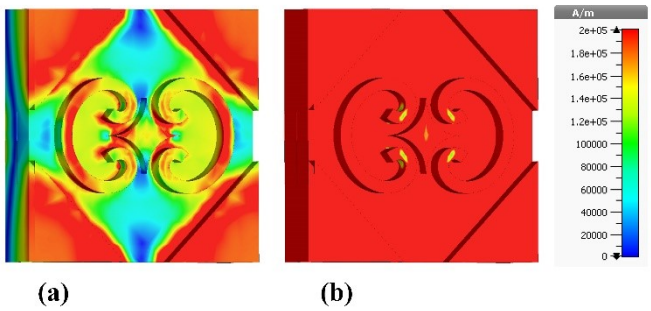

Figure 12: Magnetic field (|H|) distribution for silver resonators: (a) Real component of |H|, (b) Imaginary component of |H|.

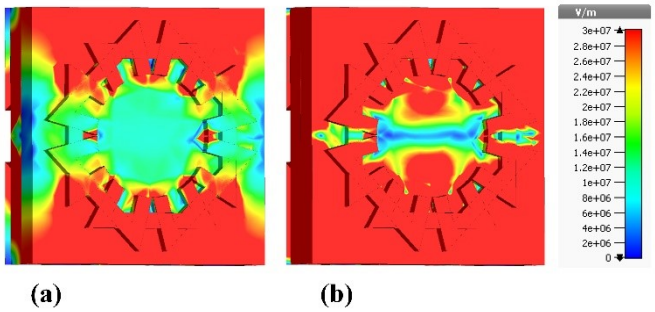

Figure 13: Rear view analysis of the nickel backplane, showing |E|-field distribution: (a) Real component, (b) Imaginary component.

Figure 14 presents the magnetic field distribution on the nickel backplane. In Figure 14(a), the real component shows strong magnetic field confinement around the structural features, reinforcing the backplane's role in enhancing resonator coupling with incoming waves. Figure 14(b) depicts the imaginary component, highlighting regions where magnetic field dissipation occurs. These areas correlate with efficient energy absorption, especially where the magnetic field interacts closely with the material.

Overall, the electric and magnetic field distributions confirm the nickel backplane's critical contribution to the absorber's functionality. By supporting strong electromagnetic field confinement and effective dissipation, it plays a central role in achieving high absorption efficiency across the terahertz spectrum.

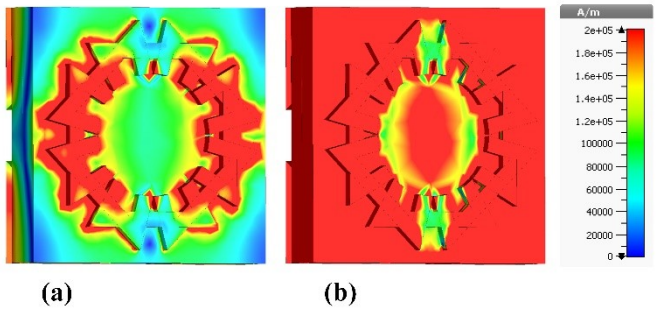

Figure 14: Rear view analysis of the nickel backplane, showing |H|-field distribution: (a) Real component, (b) Imaginary component.

B. Analysis of Surface Current and Angular Dependence

Figure 15(a) illustrates the current distribution associated with the resonators' inductive and conductive behavior. The current is concentrated along the edges and intricate features of the silver resonators, indicating regions of maximum energy flow and strong resonant interaction with incident terahertz waves. Figure 15(b) shows the imaginary component of the current, representing the dissipative or reactive behavior, which is critical for energy absorption. Areas with intense imaginary currents correspond to zones of significant energy dissipation, contributing directly to the absorber's high efficiency. These visualizations highlight the silver resonators' role in enabling strong electromagnetic coupling and effective absorption—key to optimal performance in the terahertz frequency range. The detailed current distribution patterns underscore the synergy between design geometry and material properties in maximizing operational efficiency.

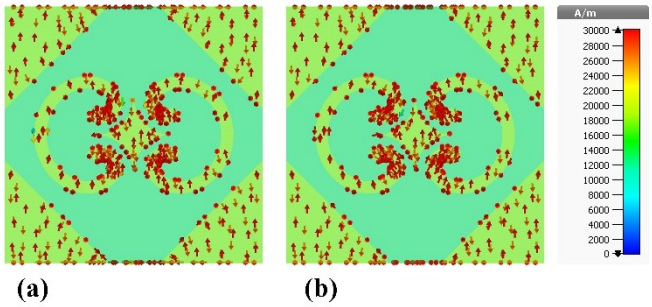

Figure 15: Visualization of surface current distribution on the silver resonators: (a) Real part of the current, (b) Imaginary part of the current.

Figure 16(a) presents the real component of the surface current on the nickel backplane, depicting conductive current flow. The distribution shows current concentrated around the backplane's intricate geometric features, facilitating efficient electromagnetic interaction and reflection. Figure 16(b) illustrates the imaginary component, which represents reactive current behavior associated with energy dissipation. Intense current regions in this plot confirm the nickel layer's important role in maximizing absorption. Together, these analyses demonstrate how the nickel backplane supports both effective energy coupling and dissipation, reinforcing its essential contribution to the absorber's high performance. The distinct current patterns further emphasize the interplay between structural design and material selection in achieving efficient broadband absorption.

Figure 17 evaluates the absorber's performance under angular variations, focusing on incident and polarization angles. Figure 17(a) shows absorption efficiency across a range of incident angles and frequencies. The plot reveals that the absorber maintains nearly perfect absorption approaching 1.0 for incident angles up to approximately 70°, with only a gradual decline beyond that. This indicates strong angular robustness and adaptability under varying incidence conditions.

Figure 17(b) illustrates the absorber's performance as a function of polarization angle. The uniform color distribution across the plot signifies that absorption efficiency remains consistent regardless of polarization orientation, confirming the polarization-insensitive nature of the design.

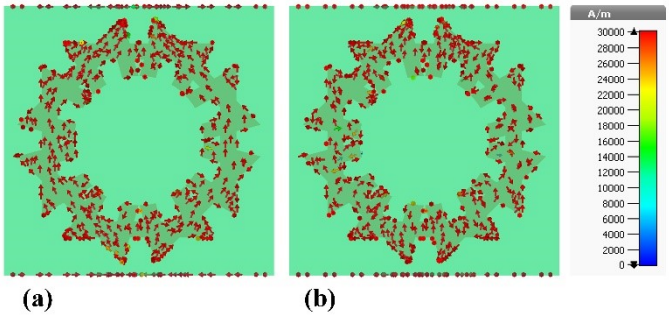

Figure 16: Surface current mapping on the nickel backplane: (a) Real component, (b) Imaginary component.

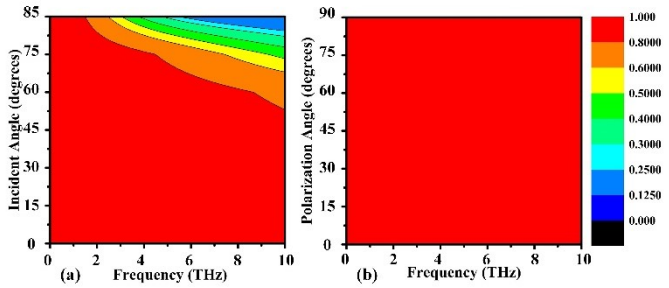

Figure 17: Absorption efficiency as a function of angle: (a) Variations in incident angle, (b) Changes in polarization angle.

These results collectively demonstrate the absorber's versatility and reliability, maintaining high performance across a broad range of operational conditions. Its robustness to incident and polarization angle variations makes it a promising candidate for practical applications in terahertz sensing, particularly in biomedical diagnostics and non-invasive detection.

VI. Feasibility of Fabricating the Proposed Nano-Metamaterial Absorber

The proposed nano-metamaterial absorber, while designed for high electromagnetic performance, has also been intentionally engineered for fabrication feasibility using current and emerging nanofabrication technologies. The structure employs well-established materials such as silver (Ag), silicon dioxide (SiO_2), titanium dioxide (TiO_2), and nickel (Ni) all of which are compatible with conventional deposition and patterning techniques. Thin films with thicknesses of 5–10 nm, as used in the absorber design, can be accurately deposited using atomic layer deposition (ALD), sputtering, or electron-beam evaporation, which are standard in semiconductor and nanophotonic fabrication processes. Nanoscale patterning of the absorber's resonators, which range from 30 to 56 nm in feature size, is achievable via electron beam lithography (EBL) or focused ion beam (FIB) milling—tools that provide sub-10 nm resolution and are widely available in academic and commercial nanofabrication facilities.

For large-scale production beyond the prototyping stage, scalable and cost-effective techniques such as nanoimprint lithography (NIL) present a viable solution. NIL enables high-throughput replication of nanoscale patterns over large wafer areas using reusable molds and is particularly suitable for the absorber's planar architecture. Furthermore, roll-to-roll nanofabrication offers an emerging path for continuous production on flexible substrates, making the design amenable to integration into disposable point-of-care diagnostic platforms. Directed self-assembly (DSA) techniques, which allow for bottom-up formation of nanoscale patterns with excellent uniformity, are also promising for mass manufacturing in cases where extreme pattern density and scalability are required.

Importantly, despite its advanced functionality, the structural design of the absorber avoids unnecessary fabrication complexity. The configuration follows a planar, layered layout without the need for high-aspect-ratio features, vertical vias, or suspended membranes. The geometry of the resonators, composed of C-shaped, triangular, and cross-shaped elements, is designed to be both functionally effective and lithographically straightforward. Each layer in the stack (resonators, dual substrates, and backplane) can be fabricated in sequential steps without requiring advanced multi-level alignment or sacrificial layer processing, thus supporting reliable and reproducible manufacturing.

The nanoscale footprint of the unit cell ($100 \times 100 \times 30$ nm^3) makes the absorber particularly well-suited for dense integration into lab-on-chip biosensing systems. It enables the formation of high-density sensor arrays capable of multiplexed biomarker detection and facilitates compatibility with microfluidic platforms for sample delivery. Additionally, the absorber's polarization-insensitive behavior and broad terahertz operational range (0.1–10 THz) significantly reduce the optical alignment constraints in practical systems, enhancing the potential for integration into compact, portable diagnostic devices.

While challenges such as film uniformity, defect control, and pattern fidelity over large areas are inherent in nanoscale fabrication, these can be mitigated through established process optimization strategies. For instance, chemical-mechanical planarization (CMP) can ensure surface smoothness, and hard-mask etching combined with optimized resist profiles can improve pattern transfer quality. Protective dielectric coatings, such as thin Al_2O_3 films deposited by ALD, can also be used to enhance environmental stability of sensitive layers like Ag without adversely affecting the absorber's performance.

VII. Diagnosis of Circulating Cancer Exosomes

The detection and diagnosis of circulating cancer exosomes represent a transformative advancement in early cancer detection. These nanoscale vesicles, secreted by tumor cells, carry molecular signatures that reflect their cellular origin, making them valuable biomarkers for non-invasive diagnostics. This section explores how the proposed nano-metamaterial biosensor utilizes advanced electromagnetic field interactions to differentiate between normal and cancerous exosomes. Through distinct electric and magnetic field responses, the biosensor demonstrates high sensitivity and specificity,

offering a promising tool for early-stage cancer diagnosis and monitoring.

Figure 18 illustrates the nano-metamaterial biosensor and its interaction with both cancerous and normal exosomes. The biosensor is designed as a multi-layered structure that enhances sensitivity to exosomal biomarkers. Cancerous exosomes, shown as red spheres, interact strongly with the sensor due to its efficient electric and magnetic field confinement. The schematic highlights how the metamaterial structure couples electromagnetic waves to exosomal particles, improving detection sensitivity and supporting the sensor's capability in non-invasive biomedical applications.

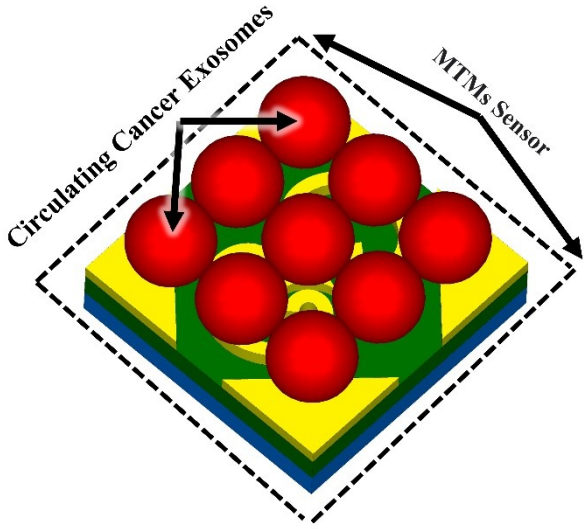

Figure 18: Schematic of the nano-metamaterial biosensor, illustrating the electric and magnetic field interactions with circulating cancerous and normal exosomes.

Figure 19 presents the biosensor's performance in distinguishing between circulating cancerous and normal exosomes across the 0.1–10 THz range. Figure 19(a) shows the electric field (E-field) response, where cancerous (red line) and normal (blue line) exosomes produce clearly distinct field magnitudes. Similarly, Figure 19(b) illustrates the magnetic field (H-field) response, with significant separation in values between the two exosome types. These differences highlight the biosensor's ability to detect unique electromagnetic signatures, confirming its effectiveness in exosome classification..

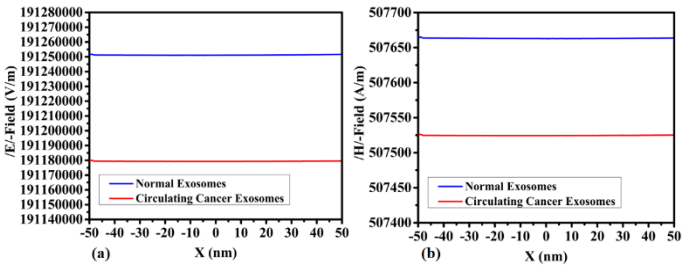

Figure 19: Biosensor performance across the 0.1–10 THz spectrum, differentiating exosome types: (a) Electric field (E-field) response, (b) Magnetic field (H-field) response.

Further insights are provided through electric field distribution analyses. Figure 20(a) displays the E-field around normal exosomes, characterized by low intensity and surface-localized interactions. The uniform blue coloration reflects minimal coupling with the metamaterial sensor. In contrast, Figure 20(b) reveals the E-field around cancerous exosomes, showing significantly stronger field intensities with red and green regions concentrated near the exosome surface. This enhanced interaction is attributed to variations in dielectric properties and molecular composition.

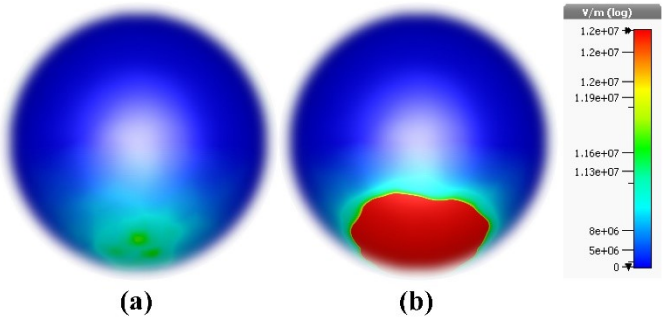

Figure 20: Visualization of the electric field for exosome imaging: (a) Normal exosomes, (b) Cancerous exosomes.

These electromagnetic differences are supported by the distinct refractive indices and dielectric constants of exosomes. Normal exosomes typically exhibit refractive indices between 1.37–1.40 and dielectric constants (εr) ranging from 3 to 5. Cancer-derived exosomes, however, present higher values, with refractive indices from 1.40–1.45 and dielectric constants between 7 and 10 [52–58]. These variations, resulting from tumor-related molecular changes, serve as reliable biomarkers for biosensing.

By leveraging these dielectric differences, the nano-metamaterial biosensor demonstrates exceptional sensitivity in detecting and distinguishing exosome types. This enhances its potential for non-invasive cancer biomarker detection, supporting advancements in early diagnostics and precision medicine.

Figure 21(a) shows the magnetic field distribution around normal exosomes, with relatively weak and uniform field intensity indicated by blue-green coloration. This suggests minimal interaction with the sensor's magnetic response. In contrast, Figure 21(b) highlights the magnetic field around cancerous exosomes, featuring higher intensities and distinctive patterns. Bright green and red regions indicate strong coupling and elevated electromagnetic absorption, likely due to unique magnetic or molecular properties.

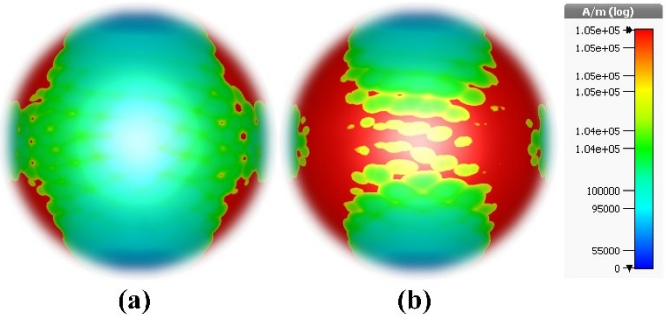

Figure 21: Visualization of the magnetic field for exosome imaging: (a) Normal exosomes, (b) Cancerous exosomes.

These simulation results reinforce the sensor's ability to differentiate between cancerous and normal exosomes based on magnetic responses, confirming its value as a precise, non-invasive diagnostic tool for early-stage cancer detection.

VIII. Benchmarking

In this section, we highlight the key features and advantages of the proposed dual-substrate nano-metamaterial absorber with negative permittivity for terahertz (THz) biosensing particularly for early cancer detection via circulating exosomes. The performance metrics below demonstrate the design's effectiveness across the 0.1–10 THz frequency range. A summary of these features is presented in Tables 2 to 5.

A. High Absorption Efficiency

The proposed absorber achieves an exceptional absorption efficiency exceeding 92% across the full 0.1–10 THz spectrum. This high efficiency maximizes the interaction between THz radiation and the material, ensuring optimal energy absorption. Its broad frequency coverage enhances the sensor's versatility for various THz biosensing applications.

B. Advanced Material Selection and Design

The design features a carefully selected combination of materials and structural elements:

- 5 nm silver (Ag) resonators enable strong plasmonic resonance, crucial for high sensitivity at THz frequencies.
- A dual-substrate configuration using 10 nm silicon dioxide (SiO_2) and 10 nm titanium dioxide (TiO_2) enhances electromagnetic wave confinement and improves overall absorption.
- A 5 nm nickel (Ni) ground plane contributes to impedance matching and absorption efficiency.

These material and geometric optimizations result in a high-performance absorber suitable for wideband THz applications.

C. Polarization Insensitivity

A key advantage of the design is its polarization-insensitive response. The sensor maintains consistent performance regardless of the polarization state of incident THz waves. This is particularly valuable in real-world biosensing environments, where the polarization of incoming radiation may vary. This feature ensures stable and reliable sensor operation across diverse experimental conditions.

D. Negative Permittivity for Enhanced Sensitivity

At 4.85 THz, the absorber exhibits negative permittivity ($\varepsilon < 0$) a property that significantly enhances its sensitivity to small changes in the refractive index of biological samples, such as exosomes. Negative permittivity facilitates stronger coupling between THz waves and the target biomarkers, enabling more robust signal detection. This is especially beneficial for identifying low-concentration biomarkers associated with early-stage cancer.

E. Optimized for Early Cancer Detection via Circulating Exosomes

The sensor is specifically tailored for the detection of circulating exosomes, nano-sized vesicles that carry key molecular markers indicative of early cancer. The ability to detect these biomarkers with high sensitivity and across a wide frequency range represents a significant advance in non-invasive diagnostic technology. Its performance makes the proposed sensor a strong candidate for early-stage cancer detection and related biomedical applications.

F. Noise Minimization

The unique dual-substrate design of the nano-metamaterial absorber plays a key role in minimizing signal noise, one of the primary challenges in THz biosensing. By leveraging negative permittivity and the hybrid resonator-substrate configuration, the sensor significantly reduces background interference, resulting in cleaner and more accurate signal acquisition. This reduction in noise is critical for improving the precision and reliability of early cancer detection, where clear differentiation between normal and cancerous exosomes is essential.

Table 2: Material and Structural Features of the Proposed Absorber

Feature	Proposed Design Details	Significance
Frequency Range	0.1–10 THz	The ideal terahertz range for early-stage cancer detection, 0.1–10 THz, excels at analyzing tissue molecular properties.
Absorption Efficiency	>92%	High energy absorption across the range ensures effective biosensing.
Resonator Material	Silver (5 nm)	Strong plasmonic response critical for THz resonance.
Substrate 1	SiO_2 (10 nm)	Optimizes wave interaction and improves absorption.
Substrate 2	TiO_2 (10 nm)	Enhances sensor stability and performance.
Ground Material	Nickel (5 nm)	Unique choice improves impedance matching and noise reduction.
Polarization Sensitivity	Insensitive	Reliable operation under varying polarization states.
Negative Permittivity	Achieved at 4.85 THz	Improves sensitivity to biological samples like exosomes.

G. Comparative Analysis

The proposed nano-metamaterial THz biosensor demonstrates significant advantages over existing designs, particularly for early-stage cancer detection via circulating exosomes. As summarized in Tables 4 and 5, it operates across a broad frequency range of 0.1–10 THz, outperforming sensors with narrower ranges such as Sensor A (2.54–5.54 THz) and Sensor D (0.80–1.87 THz) [55], [56]. This wide bandwidth enables comprehensive analysis of molecular properties, making it especially suitable for biomedical applications.

The sensor achieves an absorption efficiency exceeding 92%, on par with or surpassing leading designs like Sensor A (>90%) and Sensor D (>99%) [55], [60]. Its dual-substrate design (SiO_2 and TiO_2) enhances wave interaction, absorption efficiency, and stability—whereas most competitors, such as Sensor A and B, use single-substrate configurations that lack this optimization [55], [57].

In terms of compactness, the proposed sensor's ultra-thin structure comprising 5 nm silver, 10 nm SiO_2, 10 nm TiO_2, and 5 nm nickel greatly outperforms bulkier alternatives such as Sensor A (24,000 nm total thickness) and Sensor G (75,000 nm) [55], [58]. Its unit cell size of 100 × 100 × 30 nm allows for easy integration with microelectronic and biomedical platforms, unlike macro-scale sensors such as [55] and [26].

A key innovation is the achievement of negative permittivity at 4.85 THz, absent in all compared designs. This enables enhanced sensitivity to nanoscale biomarkers like exosomes, a feature missing from general-purpose sensors [55], [56]. Additionally, the sensor exhibits significant noise reduction, outperforming designs with only moderate noise control [55], [59].

The sensor is also polarization-insensitive, ensuring reliable operation under varying polarization states—a trait it shares with most leading designs [55], [60], but with greater stability due to its material configuration.

While Sensor [61] operates over a slightly wider range (0.1–16 THz), its larger 15.9 THz bandwidth sacrifices specificity. In contrast, the proposed sensor's 9.9 THz bandwidth is more targeted, maintaining both efficiency and sensitivity. Moreover, the proposed sensor's nano-scale footprint contrasts sharply with Sensor [55] (24,000 × 24,000 × 10,000 nm) and Sensor [26] (30,000 × 30,000 × 20,000 nm), offering a significant advantage in portability and device integration.

TABLE 3: PERFORMANCE METRICS OF THE PROPOSED ABSORBER

Metric	Proposed Design Performance	Description
Absorption Bandwidth	0.1–10 THz	A wide range, especially between 0.1 and 10 THz, ensures compatibility with various biomarkers.
Absorption Efficiency	>92%	Demonstrates high absorption across the entire operational range.
Noise Reduction	Significant	Optimized material and structural design minimize signal noise for clearer detection.
Sensitivity	Enhanced by negative permittivity	Capable of detecting low-concentration biomarkers in early cancer stages.
Application Focus	Early cancer detection via circulating exosomes	Specifically tailored for accurate biosensing.
Resonator Configuration	Dual substrate (SiO_2 & TiO_2) with silver resonators	Hybrid structure maximizes performance and reliability.
Polarization Dependence	Polarization-insensitive	Ensures consistent operation under varying incident wave polarizations.

Material selection also distinguishes this design: Ag, SiO_2, TiO_2, and Ni provide strong plasmonic resonance, stability, and noise reduction. Competing designs using graphene or gold (Au) [60], [6] may offer good conductivity but lack specialized performance for nano-scale exosome detection.

Critically, this is the only sensor specifically designed to detect circulating cancer exosomes. Competing sensors are generalized and do not provide optimized electromagnetic interactions for exosome detection. The combination of negative permittivity, broad THz range, and nano-scale precision allows the proposed sensor to exceed the capabilities of broader-use designs such as [59] and [61].

In terms of bandwidth, the sensor's 9.9 THz range surpasses several others, including [55] (3 THz) and [63] (2.5 THz), while maintaining low noise and high sensitivity. Although Sensor [62] offers a slightly larger bandwidth (10.76 THz), it is limited by higher noise levels and lacks specificity for exosomes. The compact, nano-scale design of the proposed sensor ensures seamless integration into portable biomedical diagnostic devices, giving it a clear edge in practical applications.

IX. FUTURE PERSPECTIVE

The proposed THz nano-metamaterial absorber represents a transformative step in early cancer detection and paves the way for next-generation biosensing technologies. Future research should aim to optimize the device for broader clinical use, including multi-biomarker detection and advanced disease staging. Integrating machine learning algorithms with the sensor's high sensitivity and specificity could enable real-time data analysis and predictive diagnostics, enhancing its role in personalized medicine.

To expand biomedical applicability, miniaturizing the sensor within integrated lab-on-chip systems is a critical next step. This would enable portable, point-of-care diagnostic devices capable of detecting exosomes and other nanoscale biomarkers directly from biological fluids, offering a major leap in non-invasive diagnostics, especially in resource-limited settings.

Material innovation also has potential to boost performance. While the current design utilizes Ag, SiO_2, TiO_2, and Ni for their favorable properties, exploring emerging metamaterials and hybrid plasmonic-quantum systems could further improve sensitivity and reduce noise. Additionally, expanding the operational frequency range beyond 10 THz could facilitate detection of a wider array of biomarkers, creating a more comprehensive diagnostic platform.

Finally, clinical validation through in-vivo testing is essential to confirm the sensor's efficacy and safety in real-world settings. Collaboration with oncologists and healthcare institutions will be key to accelerating clinical adoption. With continued development, the proposed sensor could redefine early cancer diagnostics, enable the next generation biosensing, and contribute to improved patient outcomes and reduce global healthcare costs.

X. CONCLUSIONS

The proposed nano-metamaterial THz biosensor introduces a transformative approach to early cancer detection by enabling the precise and sensitive identification of circulating cancer exosomes. Operating across a broad frequency range of 0.1–10 THz, it addresses the critical need for detailed molecular analysis in the terahertz domain, making it well-suited for biomedical applications. With an absorption efficiency exceeding 92%, the sensor ensures robust detection of subtle electromagnetic interactions associated with nanoscale biomarkers. Its compact nano-scale design (100 × 100 × 30 nm) significantly outperforms the bulkier, micron-scale alternatives, facilitating integration into portable diagnostic devices.

The sensor's construction—using Ag, SiO_2, TiO_2, and Ni—is key to its superior performance. The silver layer enables strong plasmonic resonance, while the dual substrates enhance wave interaction, structural stability, and absorption. The nickel backplane provides impedance matching and minimizes signal noise. Additionally, the sensor achieves negative permittivity at 4.85 THz, allowing precise differentiation between normal and cancerous exosomes. This level of specificity is critical for early-stage cancer diagnostics something conventional THz sensors struggle to achieve.

The design also addresses common challenges in the field. Polarization insensitivity ensures consistent performance regardless of the incident wave's polarization, and low noise levels improve detection accuracy, increasing the sensor's reliability in practical applications. In contrast, existing sensors (see Tables 4 and 5) often suffer from higher noise, narrower frequency ranges, and limited sensitivity to nanoscale biomarkers.

With a competitive 9.9 THz bandwidth, the sensor strikes a balance between wide operational range and high precision. Unlike some broader-band sensors that compromise on signal quality, this design maintains performance while enabling the detection of key cancer biomarkers such as exosomes. Its non-invasive detection capabilities offer a significant advance in early diagnostics, with the potential to improve patient outcomes and reduce healthcare costs.

The proposed THz biosensor stands out through its compact form factor, innovative material integration, low noise, and targeted exosome detection. Purpose-built for early cancer diagnostics, it sets a new benchmark for sensitivity and specificity in THz biosensing. Beyond cancer detection, this platform holds promise for broader applications in molecular characterization and real-time biosensing, marking a significant step forward in non-invasive diagnostic technologies.

XI. Road Map for Experimental Validation and Specificity Assessment

The practical application of the proposed THz nano-metamaterial absorber for cancer diagnostics hinges not only on its theoretical performance but also on experimental validation under realistic biological conditions. While the current study focuses on comprehensive electromagnetic simulations and structural optimization, the next phase of this research will involve systematic experimental efforts to fabricate, characterize, and biologically validate the sensor. A structured roadmap has been formulated to bridge the gap between theoretical promise and real-world deployment.

The fabrication process will employ established nanofabrication techniques such as electron beam lithography (EBL) for patterning the silver resonators, and atomic layer deposition (ALD) or sputtering for thin-film deposition of SiO_2, TiO_2, and Ni layers. The use of standard silicon or quartz wafers will support CMOS compatibility and facilitate integration into microfluidic platforms. After fabrication, characterization of the absorber's electromagnetic response will be conducted using terahertz time-domain spectroscopy (THz-TDS), providing direct measurement of absorption spectra across the 0.1–10 THz range and enabling comparison with simulation results.

To simulate realistic sensing conditions, we have already incorporated biologically relevant optical properties into our electromagnetic models. Specifically, cancerous exosomes are characterized by slightly elevated refractive indices (1.40–1.45) and dielectric constants ($\varepsilon_r \approx 7$–10), whereas normal exosomes exhibit lower values (1.37–1.40; $\varepsilon_r \approx 3$–5). These parameters were used to generate distinct electromagnetic signatures, demonstrating the sensor's ability to differentiate between cancerous and normal exosomes. In Figures 19–21, the spatial electric and magnetic field distributions confirm strong localized resonance for cancerous exosomes, with weaker responses observed for non-cancerous ones. This result substantiates the sensor's high specificity under modeled conditions and provides a compelling basis for further in vitro testing.

Biological testing will involve isolating exosomes from clinical plasma samples using differential centrifugation and immunoaffinity capture techniques. These samples will then be introduced into the sensing platform using a microfluidic interface designed to concentrate analytes over the active sensing surface. Real-time monitoring via THz-TDS will be used to detect and quantify shifts in absorption characteristics corresponding to the interaction with different types of exosomes. By analyzing the spectral and field response, we aim to determine the sensor's ability to distinguish cancer-specific biomarkers from the heterogeneous background of biological vesicles and proteins.

Addressing the issue of specificity, the proposed design incorporates several inherent features that improve selectivity and suppress noise. The negative permittivity achieved at 4.85 THz allows the sensor to exhibit heightened sensitivity to small permittivity shifts in the surrounding medium, which are characteristic of cancerous exosomes. Moreover, the strong field confinement enabled by the plasmonic Ag resonators ensures localized interaction at the sensor surface, minimizing interference from non-target particles. The dual-substrate configuration of SiO_2 and TiO_2 contributes to enhanced impedance matching and reduced background reflection, thereby maximizing signal clarity. Our simulations demonstrate minimal reflectivity (< -10 dB) and negligible transmission ($< 0.2\%$) across the target band, indicating high energy absorption and a robust signal-to-noise ratio.

To further improve signal fidelity, the integration of pre-sensing purification steps—such as size-exclusion filtration or antibody-based capture—will be considered in the final prototype design. These steps will reduce the presence of non-exosomal vesicles and ensure that only target particles interact with the sensing surface, enhancing diagnostic specificity. Future work will also explore machine learning-based classification of THz spectral patterns to automate and improve the differentiation of exosomal subtypes.

Competing interests

The authors declare no competing interests.

Data availability

The datasets used and/or analyzed during the current study are available from the corresponding author on reasonable request.

TABLE 4: COMPARISON OF THZ BIOSENSORS FOR EARLY CANCER DETECTION (0.1–10 THZ)

Parameter	Proposed Sensor	Sensor A [55]	Sensor B [57]	Sensor C [60]	Sensor D [56]	Sensor E [64]	Sensor F [63]	Sensor G [58]
Frequency Range (THz)	0.1–10	2.54–5.54	3.05–8.14	2.34 –5.64	0.80–1.87	3.01–7.27	7–9.5	2.7–5.7
Absorption Efficiency (%)	>92%	>90 %	>90 %	>90 %	> 99%	>90 %	>90 %	>90 %
Substrate Design	Dual substrate (SiO_2 and TiO_2)	Single	Single	Single	Single	Single	Single	Single
Thickness of Components (nm)	5 nm (silver), 10 nm (SiO_2, TiO_2), 5 nm (nickel)	24,000 nm (Vo2), 24,000 nm (Polyimide), 10,000 nm (Au)	28,000 nm (Vo2), 28,000 nm (Quartz), 8,200 nm (Au)	30,000 nm (Vo2), 30,000 nm (SiO_2), 9,200 nm (Au)	33,000 nm (Graphene), 33,000 nm (polyimide), 36,000 nm (Au)	24,000 nm (Vo2), 24,000 nm (SiO_2), 7,000 nm (Au)	25,000 nm (Graphene), 25,000 nm (SiO_2), 25,000 nm (Au)	75,000 nm (Vo2), 75,000 nm (Quartz), 11,000 nm (Au)
Negative Permittivity	Observed at 4.85 THz	not observed	not observed	not observed	not observed	not observed	not observed	not observed
Sensitivity to Exosomes	High	Low, due to the nano-scale size of exosomes	Low, due to the nano-scale size of exosomes	Low, due to the nano-scale size of exosomes	Low, due to the nano-scale size of exosomes	Low, due to the nano-scale size of exosomes	Low, due to the nano-scale size of exosomes	Low, due to the nano-scale size of exosomes
Polarization Insensitivity	Yes	Yes	Yes	Yes	Yes	Yes	Yes	Yes
Noise Reduction	Significant	Moderate	Moderate	Moderate	Low	Moderate	Moderate	Moderate
Application Focus	Early cancer detection via circulating exosomes	General-purpose	General-purpose	General-purpose	General-purpose	General-purpose	General-purpose	General-purpose

TABLE 5: COMPARATIVE ANALYSIS WITH RELEVANT WORK

Ref.	Operation Range (THz)	Unit cell Dimension (nm)	Materials	Bandwidth (THz)	Size Scale	Noise Level	Exosome Detection Capability
[55]	2.54–5.54	24,000 × 24,000 × 10,000	Vo2,Polyimide,Au	3	Micron	Moderate	No
[59]	8.5–11	35,000 × 35,000 × 13,850	Vo2, SiO_2, Au	2.5	Micron	High	No
[57]	3.05–8.14	28,000 × 28,000 × 8,200	Vo2, Quartz, Au	5.09	Micron	Moderate	No
[60]	2.34 –5.64	30,000 × 30,000 × 9,200	Vo2, SiO_2, Au	3.30	Micron	Moderate	No
[56]	0.80–1.87	33,000 × 33,000 × 36,000	Graphene, Polyimide, Au	1.07	Micron	High	No
[62]	1.63–12.39	30,000 × 30,000 × 20,000	Vo2, Topas, Au	10.76	Micron	High	No
[65]	1.75–5	55,000 × 55,000 × 15,000	ITO, PET	3.25	Micron	Moderate	No
[63]	7–9.5	25,000 × 25,000 × 25,000	Graphene, SiO_2, Au	2.5	Micron	Moderate	No
[64]	3.01–7.27	24,000 × 24,000 × 7,000	Vo2, SiO_2, Au	4.26	Micron	Moderate	No
[58]	2.7–5.7	75,000 × 75,000 × 11,000	Vo2, Quartz, Au	3	Micron	Moderate	No
[61]	0.1–16	40,000 × 40,000 × 870,000	ECCOSORB AN-72, SiO_2, Ni	15.9	Micron	High	No
This work	0.1–10	100 × 100 × 30	Ag, SiO_2, TiO_2,Ni	9.9	Nano	Low	Yes

REFERENCES

[1] F. Bray, J. Ferlay, I. Soerjomataram, R. L. Siegel, L. A. Torre, and A. Jemal, "Global cancer statistics 2018: GLOBOCAN estimates of incidence and mortality worldwide for 36 cancers in 185 countries," *CA: a cancer journal for clinicians,* vol. 68, no. 6, pp. 394-424, 2018.

[2] W. Cao, H.-D. Chen, Y.-W. Yu, N. Li, and W.-Q. Chen, "Changing profiles of cancer burden worldwide and in China: a secondary analysis of the global cancer statistics 2020," *Chinese medical journal,* vol. 134, no. 07, pp. 783-791, 2021.

[3] N. Pashayan and P. D. Pharoah, "The challenge of early detection in cancer," *Science,* vol. 368, no. 6491, pp. 589-590, 2020.

[4] N. A. Hanjani *et al.*, "Emerging role of exosomes as biomarkers in cancer treatment and diagnosis," *Critical reviews in oncology/hematology,* vol. 169, p. 103565, 2022.

[5] Q. Maqsood, A. Sumrin, Y. Saleem, A. Wajid, and M. Mahnoor, "Exosomes in Cancer: Diagnostic and Therapeutic Applications," *Clinical Medicine Insights: Oncology,* vol. 18, p. 11795549231215966, 2024.

[6] M. D. A. Paskeh *et al.*, "Emerging role of exosomes in cancer progression and tumor microenvironment remodeling," *Journal of hematology & oncology,* vol. 15, no. 1, p. 83, 2022.

[7] W. Yu *et al.*, "Exosome-based liquid biopsies in cancer: opportunities and challenges," *Annals of Oncology,* vol. 32, no. 4, pp. 466-477, 2021.

[8] M. Ghodrati and A. Uniyal, "Exploring Metasurface-Based Biosensor: New Frontiers in Sensitivity and Versatility for Biomedical Applications," *Plasmonics,* pp. 1-20, 2024.

[9] Q. Zhao, J. Zhou, F. Zhang, and D. Lippens, "Mie resonance-based dielectric metamaterials," *Materials today,* vol. 12, no. 12, pp. 60-69, 2009.

[10] M.-R. Nickpay, M. Danaie, and A. Shahzadi, "Graphene-based tunable quad-band fan-shaped split-ring metamaterial absorber and refractive index sensor for THz spectrum," *Micro and Nanostructures,* vol. 173, p. 207473, 2023.

[11] H. Kim and J. Hopwood, "Wave propagation in composites of plasma and metamaterials with negative permittivity and permeability," *Scientific Reports,* vol. 9, no. 1, p. 3024, 2019.

[12] C. Tan *et al.*, "Cancer Diagnosis Using Terahertz-Graphene-Metasurface-Based Biosensor with Dual-Resonance Response," *Nanomaterials,* vol. 12, no. 21, p. 3889, 2022.

[13] M. Y. Azab, M. F. O. Hameed, A. M. Nasr, and S. Obayya, "Highly sensitive metamaterial biosensor for cancer early detection," *IEEE Sensors Journal,* vol. 21, no. 6, pp. 7748-7755, 2021.

[14] M. N. Hamza *et al.*, "Designing a High-sensitivity Microscale Triple-band Biosensor based on Terahertz MTMs to provide a perfect absorber for Non-Melanoma Skin Cancer diagnostic," *IEEE Photonics Journal,* 2024.

[15] S. K. Patel, J. Surve, and J. Parmar, "Detection of cancer with graphene metasurface-based highly efficient sensors," *Diamond and Related Materials,* vol. 129, p. 109367, 2022.

[16] B. Amini and Z. Atlasbaf, "Design and analysis of high-sensitivity tunable graphene sensors for cancer detection," *Optical and Quantum Electronics,* vol. 55, no. 5, p. 446, 2023.

[17] M. N. Hamza and M. T. Islam, "Design of MTM-based Multi-band Micro-Biosensor in Terahertz region as perfect absorber for

Early-Stage Leukemia Diagnosis with sensitivity 18626373 THz/RIU," *IEEE Sensors Journal,* 2024.
[18] P. Upender and A. Kumar, "THz dielectric metamaterial sensor with high Q for biosensing applications," *IEEE Sensors Journal,* vol. 23, no. 6, pp. 5737-5744, 2023.
[19] M. N. Hamza, S. Koziel, and A. Pietrenko-Dabrowska, "Design and experimental validation of a metamaterial-based sensor for microwave imaging in breast, lung, and brain cancer detection," *Scientific Reports,* vol. 14, no. 1, p. 16177, 2024.
[20] Z. Geng, X. Zhang, Z. Fan, X. Lv, and H. Chen, "A route to terahertz metamaterial biosensor integrated with microfluidics for liver cancer biomarker testing in early stage," *Scientific reports,* vol. 7, no. 1, p. 16378, 2017.
[21] S. Banerjee, U. Nath, P. Dutta, A. V. Jha, B. Appasani, and N. Bizon, "A theoretical terahertz metamaterial absorber structure with a high quality factor using two circular ring resonators for biomedical sensing," *Inventions,* vol. 6, no. 4, p. 78, 2021.
[22] H. E. Nejad, A. Mir, and A. Farmani, "Supersensitive and tunable nano-biosensor for cancer detection," *IEEE Sensors Journal,* vol. 19, no. 13, pp. 4874-4881, 2019.
[23] D. Li *et al.*, "Identification of early-stage cervical cancer tissue using metamaterial terahertz biosensor with two resonant absorption frequencies," *IEEE Journal of Selected Topics in Quantum Electronics,* vol. 27, no. 4, pp. 1-7, 2021.
[24] S. Banerjee, P. Dutta, A. V. Jha, B. Appasani, and M. S. Khan, "A biomedical sensor for detection of cancer cells based on terahertz metamaterial absorber," *IEEE Sensors Letters,* vol. 6, no. 6, pp. 1-4, 2022.
[25] M. N. Hamza and M. T. Islam, "Designing an Extremely Tiny Dual-Band Biosensor Based on MTMs in the Terahertz Region as a Perfect Absorber for Non-Melanoma Skin Cancer Diagnostics," *IEEE Access,* vol. 11, pp. 136770-136781, 2023.
[26] A. Chaudhuri, B. Rai, and P. Pal, "Design of a dual-band metasurface cross-polarization converter for cancer detection in the terahertz band," *IEEE Sensors Journal,* vol. 24, no. 6, pp. 7292-7298, 2023.
[27] J. Chen, F. Hu, X. Ma, M. Yang, S. Lin, and A. Su, "Deep neural network assisted terahertz metasurface sensors for the detection of lung cancer biomarkers," *IEEE Sensors Journal,* 2024.
[28] M. N. Hamza, M. T. Islam, S. Lavadiya, S. Koziel, I. Ud Din, and B. Sanches, "Designing a High-sensitivity Dual-band Nano-Biosensor based on Petahertz MTMs to provide a perfect absorber for Early-Stage Non-Melanoma Skin Cancer diagnostic," *IEEE Sensors Journal,* 2024.
[29] A. Hlali, A. Oueslati, and H. Zairi, "Numerical simulation of tunable terahertz graphene-based sensor for breast tumor detection," *IEEE Sensors Journal,* vol. 21, no. 8, pp. 9844-9851, 2021.
[30] X. Hou *et al.*, "Cancer biomarkers ultrasensitive detection based on terahertz frequency-comb-like," *IEEE Sensors Journal,* vol. 23, no. 10, pp. 10413-10419, 2023.
[31] M. N. Hamza *et al.*, "Development of a Terahertz Metamaterial Micro-Biosensor for Ultrasensitive Multispectral Detection of Early-Stage Cervical Cancer," *IEEE Sensors Journal,* 2024.
[32] A. Veeraselvam, G. N. A. Mohammed, K. Savarimuthu, and P. D. Vijayaraman, "An ultra-thin multiband refractive index-based carcinoma sensor using THz radiation," *IEEE Sensors Journal,* vol. 22, no. 3, pp. 2045-2052, 2021.
[33] M. N. Hamza *et al.*, "Ultra-compact quintuple-band terahertz metamaterial biosensor for enhanced blood cancer diagnostics," *PLOS ONE,* vol. 20, no. 1, p. e0313874, 2025.
[34] D. Xie *et al.*, "Terahertz metamaterial biosensor with double resonant frequencies for specific detection of early-stage hepatocellular carcinoma," *IEEE Sensors Journal,* vol. 23, no. 2, pp. 1124-1131, 2022.
[35] F. Wahaia *et al.*, "Detection of colon cancer by terahertz techniques," *Journal of Molecular Structure,* vol. 1006, no. 1-3, pp. 77-82, 2011.
[36] M. N. Hamza *et al.*, "Terahertz Dual-Band Metamaterial Biosensor for Cervical-Cancer Diagnostics," *IEEE Photonics Journal,* 2024.
[37] M. Rezeg, A. Hlali, and H. Zairi, "THz Biomedical Sensing for Early Cancer Detection: Metamaterial Graphene Biosensors with Rotated Split-Ring Resonators," *IEEE Photonics Journal,* 2024.
[38] L. Yu *et al.*, "The medical application of terahertz technology in non-invasive detection of cells and tissues: opportunities and challenges," *RSC advances,* vol. 9, no. 17, pp. 9354-9363, 2019.
[39] M. N. Hamza *et al.*, "Precision Multi-Band Terahertz Metamaterial Biosensor with Targeted Spectral Selectivity for Early Detection of MCF-7 Breast Cancer Cells," *IEEE Sensors Journal,* 2025.
[40] G. Valušis, A. Lisauskas, H. Yuan, W. Knap, and H. G. Roskos, "Roadmap of terahertz imaging 2021," *Sensors,* vol. 21, no. 12, p. 4092, 2021.
[41] M. N. Hamza, M. T. Islam, and S. Koziel, "Advanced sensor for non-invasive breast cancer and brain cancer diagnosis using antenna array with metamaterial-based AMC," *Engineering Science and Technology, an International Journal,* vol. 56, p. 101779, 2024.
[42] W. Zhang *et al.*, "Terahertz metamaterials for biosensing applications: A review," *Biosensors,* vol. 14, no. 1, p. 3, 2023.
[43] M. N. Hamza *et al.*, "Development of a High-Sensitivity Triple-Band Nano-Biosensor Utilizing Petahertz Metamaterials for Optimal Absorption in Early-Stage Leukemia Detection," *IEEE Sensors Journal,* 2025.
[44] M. N. Hamza *et al.*, "Polarization-Insensitive Nano-Metamaterial Sensor with Near-Infrared $\mu $ and $\epsilon $ Negative Properties for Early Cancer Detection via Exosome Analysis (70 THz to 3 PHz)," *IEEE Photonics Journal,* 2025.
[45] T. Kamani, S. K. Patel, O. Alsalman, and F. Alsaif, "Design and optimization of refractive index biosensor for MDA-MB-231 and MCF-7 breast cancer biomarker detection," *Physica Scripta,* vol. 99, no. 10, p. 105541, 2024.
[46] F. Dell'Olio, J. Su, T. Huser, V. Sottile, L. E. Cortés-Hernández, and C. Alix-Panabières, "Photonic technologies for liquid biopsies: recent advances and open research challenges," *Laser & photonics reviews,* vol. 15, no. 1, p. 2000255, 2021.
[47] J. Algorri *et al.*, "Polarization-independent hollow nanocuboid metasurfaces with robust quasi-bound states in the continuum," *Optical Materials,* vol. 147, p. 114631, 2024.
[48] J. Algorri *et al.*, "Experimental demonstration of a silicon-slot quasi-bound state in the continuum in near-infrared all-dielectric metasurfaces," *Optics & Laser Technology,* vol. 161, p. 109199, 2023.
[49] Q. Wang, H. Du, F. Li, and D. Ling, "Nano-Metamaterial: A State-of-the-Art Material for Magnetic Resonance Imaging," *Small Science,* vol. 3, no. 8, p. 2300015, 2023.
[50] D.-K. Lee *et al.*, "Nano metamaterials for ultrasensitive Terahertz biosensing," *Scientific reports,* vol. 7, no. 1, p. 8146, 2017.
[51] R. Zhou, C. Wang, W. Xu, and L. Xie, "Biological applications of terahertz technology based on nanomaterials and nanostructures," *Nanoscale,* vol. 11, no. 8, pp. 3445-3457, 2019.
[52] D. Hou *et al.*, "Terahertz spectroscopic investigation of human gastric normal and tumor tissues," *Physics in Medicine & Biology,* vol. 59, no. 18, p. 5423, 2014.
[53] S. P. Mickan *et al.*, "Label-free bioaffinity detection using terahertz technology," *Physics in Medicine & Biology,* vol. 47, no. 21, p. 3789, 2002.

[54] S. Smye, J. Chamberlain, A. Fitzgerald, and E. Berry, "The interaction between terahertz radiation and biological tissue," *Physics in Medicine & Biology,* vol. 46, no. 9, p. R101, 2001.
[55] C. Gandhi, P. R. Babu, and K. Senthilnathan, "Ultra-thin polarization independent broadband terahertz metamaterial absorber," *Frontiers of Optoelectronics,* vol. 14, no. 3, pp. 288-297, 2021.
[56] M. Fu, J. Wang, S. Guo, Z. Wang, P. Yang, and Y. Niu, "A polarization-insensitive broadband terahertz absorber using patterned graphene," *Nanomaterials,* vol. 12, no. 21, p. 3763, 2022.
[57] Y. Li *et al.*, "Tunable ultra-broadband terahertz perfect absorber based on vanadium oxide metamaterial," *Optics Express,* vol. 29, no. 25, pp. 41222-41233, 2021.
[58] U. U. R. Qureshi, M. I. Khan, and B. Hu, "A theoretical proposal for an actively controlled ultra-wideband absorber based on vanadium dioxide hybrid metamaterials," *Applied Sciences,* vol. 12, no. 19, p. 10164, 2022.
[59] Z. Zheng *et al.*, "Terahertz perfect absorber based on flexible active switching of ultra-broadband and ultra-narrowband," *Optics Express,* vol. 29, no. 26, pp. 42787-42799, 2021.
[60] G. Wu, X. Jiao, Y. Wang, Z. Zhao, Y. Wang, and J. Liu, "Ultra-wideband tunable metamaterial perfect absorber based on vanadium dioxide," *Optics Express,* vol. 29, no. 2, pp. 2703-2711, 2021.
[61] D. Chen, B. Xu, Z. Qiu, X. Wang, and J. Wu, "Ultra-broadband terahertz metamaterial absorber based on flexible wave-absorbing material," *Results in Physics,* vol. 52, p. 106880, 2023.
[62] P. Zhang *et al.*, "Ultra-broadband tunable terahertz metamaterial absorber based on double-layer vanadium dioxide square ring arrays," *Micromachines,* vol. 13, no. 5, p. 669, 2022.
[63] Z. Chen *et al.*, "Graphene Multi-Frequency Broadband and Ultra-Broadband Terahertz Absorber Based on Surface Plasmon Resonance," *Electronics,* vol. 12, no. 12, p. 2655, 2023.
[64] X. Wang, G. Wu, Y. Wang, and J. Liu, "Terahertz broadband adjustable absorber based on VO2 multiple ring structure," *Applied Sciences,* vol. 13, no. 1, p. 252, 2022.
[65] S. Hafeez, J. Yu, F. A. Umrani, A. Majeed, and W. Yun, "A Broadband Meta-Absorber for Curved Terahertz Stealth Applications," *Electronics,* vol. 13, no. 15, p. 2966, 2024.